Modeling variable-density flow in saturated-unsaturated porous media: An advanced numerical model

Anis Younes, Behshad Koohbor, Benjamin Belfort, Philippe Ackerer, Joanna Doummar, Marwan Fahs

Modeling variable-density flow in saturated-unsaturated porous media: An advanced numerical model

Anis Younes,[1] Behshad Koohbor,[2] Benjamin Belfort,[1] Philippe Ackerer,[1] Joanna Doummar,[3] Marwan Fahs[1*]

[1] Institut Terre et Environnement de Strasbourg, Université de Strasbourg, CNRS, ENGEES, UMR 7063

[2]BRGM (French Geological Survey), Orléans, France

[3] Department of Geology, American University of Beirut, Beirut, Lebanon

Submitted to Advances in Water Resources

Contact author: Marwan Fahs

E-mail: fahs@unistra.fr

Abstract

Modeling variable-density flow in unconfined aquifers is a challenging task because of the nonlinear coupling between variably saturated flow and contaminant transport. This results in a highly nonlinear system since the strongly nonlinear Richards flow equation is, in addition, coupled to the advection-dispersion transport equation by viscosity and density variation. The solution of such a nonlinear system is often subject to convergence issues and can be very expansive in terms of computational time, especially for large-scale problems. Conventional numerical algorithms based on the sequential approach and the classical finite difference or finite element methods with the first-order backward Euler time integration scheme are generally inefficient and/or do not provide satisfactory results. In this work, we develop a new efficient and accurate 2D numerical model for the transport of dense contaminants in unsaturated porous media that allows for the simulation of large-scale problems. This research describes a new model that combines advanced spatial discretization methods (mixed hybrid finite element method, discontinuous Galerkin finite element method, and multipoint flux approximation method) with higher-order time integration techniques via the method of lines (MOL). The latter allows one to adapt the time step's size and the order of the time integration to improve the computational efficiency while maintaining accuracy. The robustness and accuracy of the new model are shown by comparison against a widely used commercial code based on the standard finite element method. The applicability of the developed model to a large-scale problem is then investigated by simulating saltwater intrusion under a climate change projection and long-term pumping regimes for the Akkar coastal aquifer in Lebanon using a simplified 2D conceptual model.

Key words: unsaturated flow, variable-density flow, mixed finite element method, discontinuous finite element method, multi-Point flux approximation, method of lines, field simulation.

1. Introduction

Many saturated-unsaturated aquifer systems are subject to the pollution of soils and groundwater resources by dense contaminants such as leachates derived from waste disposal sites, agricultural activity, or sanitary landfills. Contamination by saltwater is a major environmental issue that occurs, for instance, with the leakage of brine beneath the salt lakes, flooding of coastal areas by seawater, saltwater intrusion in coastal aquifers due to over-pumping, tidal effects or sea-level rise. For such situations, fluid flow and solute transport equations are coupled by the fluid density.

Several studies have focused on variable-density flow in saturated porous media [1-4] since the effect of density variations on the flow behavior in the saturated zone is much more significant than in the unsaturated zone. Indeed, in the unsaturated zone, the density variation in the liquid phase is much less important than the density variation between the liquid and the air phase (about three orders of magnitude). Simmons *et al.* [5] investigated the migration of a dense contaminant plume through the unsaturated zone using laboratory experiments. They showed that the unsaturated zone and position of the water table must be considered in contamination studies in order to predict the migration pathways, rates and the ultimate fate of dense contaminant plumes [5]. Oostrom *et al.* [6] and Dane *et al.* [7] investigated saturated variable-density flow with a narrow unsaturated zone in their physical models. They showed that the development of plume instabilities depends on the density difference between the plume and groundwater, the horizontal Darcy velocity, the contaminant leakage rates, the source dimensions, the hydrodynamic dispersion and the permeability of the porous media. Ouyang and Zheng [8] numerically showed that density-driven transport is significant for dissolved chemicals through unsaturated sandy soils. Using numerical simulations, Boufadel *et al.* [9] showed that concentration-dependent viscosity effects below dry salt lakes are

84 significant under fully saturated conditions, but have minor effects under unsaturated flow
85 conditions.

86 Considering both saturated and unsaturated zones for coupled flow and transport processes
87 can improve the representativeness of simulations when investigating evaporation and salt
88 accumulation effects on riparian freshwater lenses [10] or when investigating the effect of
89 water table salinization [11-14] or the effect of the slope of the seaward boundary on saltwater
90 intrusion [15-17].

91 Including the unsaturated zone when modeling variable-density flow problems requires the
92 solution of a coupled flow-transport nonlinear system. In such a system, the flow is ruled by
93 the Richards' equation (RE), which uses nonlinear constitutive relationships between
94 hydraulic conductivity, water content, and pressure head [18, 19]. Because of these
95 nonlinearities, providing an accurate solution of RE is challenging due to convergence issues
96 and high time consumption, particularly in the presence of sharp wetting fronts, as when
97 simulating infiltration into initially dry soils [20]. These difficulties are increased in the case
98 of a dense contaminant because of additional nonlinearities induced by density variations
99 which require coupling between the RE and the advection-dispersion transport equation.

100 Because of nonlinearities and the absence of analytical solutions, numerical models are
101 valuable tools for solving these complex problems and for understanding and predicting the
102 propagation of contaminations in the aquifers. However, most of the existing numerical
103 models do not provide satisfactory results when applied to unsaturated variable-density flow
104 problems, essentially because:

105 • Classical spatial discretization methods such as finite element (FE) or finite difference
106 (FD) methods may not provide an accurate velocity field, especially in the case of
107 highly heterogeneous and/or anisotropic domains [21, 22].

- When applied to the transport equation, the classical methods provide results with significant unphysical oscillations for advection-dominated transport. If combined with first-order upstream techniques, they suffer from excessive numerical dispersion [23].

- Temporal discretization is often based on the first-order backward Euler scheme, which does not allow large time steps and, as a consequence, induces excessive computational time.

- Coupling between flow and transport equations is usually performed via a sequential approach with an empirical time-stepping technique without any control over the temporal truncation error, which may lead to inaccurate results [24].

To overcome these difficulties, in this work, we combine advanced spatial and temporal approximation methods. The flow equation is solved using the mixed hybrid finite element (MHFE) method [25]. This method simultaneously approximates both pressure and fluxes with the same order of convergence. The MHFE method is (i) locally conservative, (ii) well adapted for general unstructured meshes, and (iii) can easily handle full permeability tensors. The unknowns with the hybrid formulation are the traces of the pressure at edges/faces [26]. The lumped form of the MHFE method proposed in [27] is employed in this work to avoid spurious oscillations encountered with transient simulations in the case of sharp wetting fronts [28].

For the transport equation, the discontinuous Galerkin (DG) method is used to discretize the advection equation and combined with the multi-point flux approximation (MPFA) method for the discretization of the dispersion equation [29]. The DG method is strictly conservative at the element level. It yields accurate results for problems involving sharp fronts [30]. DG is used with an implicit time discretization that avoids (*i*) time-step limitation caused by the

Courant–Friedrichs–Lewy (CFL) condition of explicit schemes and (*ii*) the use of a slope-limiting procedure to ensure the stability of the results [29]. A discontinuous linear approximation is used for the concentration at each element of the mesh. Often, the DG degrees of freedom (DOFs) correspond to the discontinuous concentration at the nodes inside each element (see, for instance, [31, 32]). The DOFs used here are the mean concentration and the horizontal and vertical components of the concentration gradient at each element [29]. This choice allows one to imitate the upwind finite volume (FV) method when only the first equation corresponding to the mean concentration value is kept. Further, this choice of DOFs allows one to combine the DG method with MPFA for the approximation of dispersion without any operator splitting [29]. The classical methods, like FD or FV, based on two-point flux approximation (TPFA) to compute the flux between two adjacent elements, may not converge unless the grid is K-orthogonal [33]. The MPFA method calculates the flux at an element boundary using multiple surrounding elements; therefore, it is well adapted for general grids and full dispersion tensors [34].

The spatial discretization (MHFE_DG_MPFA) based upon the combination of MHFE, DG, and MPFA methods was shown to be robust and accurate for modeling variable-density flow in saturated porous media [35] and is extended in this work for unsaturated flow.

Higher-order time integration methods are used via the method of lines (MOL) to allow large time steps and improve the efficiency of the model. The flow and transport equations are solved simultaneously in a single step, which avoids slow convergence encountered with the sequential approach. The MOL allows one to adapt the time step's length and the order of the temporal discretization (up to 5 using the Backward Difference Formulas) in order to reduce the computational time while maintaining accuracy. The MOL is effective for the solution of the RE in the unsaturated zone [36] as well as for variable-density flow in saturated porous media [37]. In this work, the MOL is used for the first time for dense contaminant transport in

157 unsaturated porous media. Variable-order and variable-step size time integration are
158 performed using the DASPK [38] time solver.

159 ## 2. Governing Equations

160 Dense contaminant transport in unsaturated porous media is governed by the Darcy-
161 Buckingham's law, the mass conservation of the fluid and the advection-dispersion transport
162 equation. Assuming the Boussinesq approximation is valid, the flow in the unsaturated zone
163 can be written in terms of equivalent freshwater head, as follows:

164 $$\frac{\partial \theta}{\partial t} = \left(c(h) + S_S \frac{\theta(h)}{\theta_s} \right) \frac{\partial H}{\partial t} = -\nabla \cdot \boldsymbol{q} + q_S \tag{1}$$

165 $$\boldsymbol{q} = -k_r \boldsymbol{K} \left(\nabla H + \frac{\rho - \rho_0}{\rho_0} \nabla z \right) \tag{2}$$

166 where $c(h) = \partial\theta/\partial h$ is the specific moisture capacity [L^{-1}], S_S the specific mass storativity
167 related to head changes [L^{-1}], θ the current water content [L^3L^{-3}], θ_s the saturated water
168 content [L^3L^{-3}], $H = h + z$ the equivalent freshwater head [L], $h = \frac{P}{\rho_0 g}$ the pressure head, P
169 the pressure [Pa], z the upward vertical coordinate [L], t the time [T], $\boldsymbol{q}$ the Darcy's velocity
170 [LT^{-1}], q_S the sink term [T^{-1}], k_r the relative conductivity [-], $\boldsymbol{K} = \frac{\rho_0 g}{\mu}\boldsymbol{k}$ the hydraulic
171 conductivity tensor [LT^{-1}], ρ_0 the density of the displaced fluid [ML^{-3}], g the gravity
172 acceleration [LT^{-2}], μ the fluid dynamic viscosity [$ML^{-1}T^{-1}$], $\boldsymbol{k}$ the permeability tensor
173 dependent only on the porous medium [L^2], and ρ the fluid density [ML^{-3}].

174 The solute transport in the unsaturated zone is ruled by the advection-dispersion equation:

175 $$\frac{\partial(\theta C)}{\partial t} + \nabla.(\boldsymbol{q}C) - \nabla.(\boldsymbol{D}\nabla C) = q_S C \tag{3}$$

176 where C [-] is the scaled concentration and $\boldsymbol{D}$ the dispersion tensor given by:

177 $$\boldsymbol{D} = D_m \boldsymbol{I} + (\alpha_L - \alpha_T)\boldsymbol{q} \otimes \boldsymbol{q} / |\boldsymbol{q}| + \alpha_T |\boldsymbol{q}| \boldsymbol{I} \tag{4}$$

178 with α_L and α_T the longitudinal and transverse dispersivities [L], D_m the pore water
179 diffusion coefficient [L^2T^{-1}], and $\boldsymbol{I}$ the unit tensor.

180 We use the standard van Genuchten [39] model to define the relation between water content
181 and pressure head:

182 $$S_e = \frac{\theta(h) - \theta_r}{\theta_s - \theta_r} = \begin{cases} \dfrac{1}{\left(1 + (\alpha|h|)^n\right)^m} & h < 0 \\ 1 & h \geq 0 \end{cases} \tag{5}$$

183 where α [L^{-1}] and n [-] are the van Genuchten parameters, $m = 1 - 1/n$, S_e [-] the effective
184 saturation, and θ_r the residual water content [L^3L^{-3}].

185 The conductivity-saturation relationship is analytically derived from the Mualem [40] model,
186 as proposed by van Genuchten [39]:

187 $$k_r = S_e^{1/2}\left[1 - \left(1 - S_e^{1/m}\right)^m\right]^2. \tag{6}$$

188 Darcy velocity $\boldsymbol{q}$ in equation (2) depends on both the pressure head h and the concentration
189 C.

190 The flow and transport equations are coupled by the state equations. In the case of salt
191 contamination, we can use the polynomial approximations given in [1]:

192 $$\rho = \rho_0 + (\rho_1 - \rho_0)C, \text{ and } \mu = \mu_0(1.0 + 0.4819C - 0.2774C^2 + 0.7814C^3) \quad (7)$$

193 where ρ_0 and ρ_1 are densities of freshwater and saltwater and μ_0 the freshwater viscosity.
194 Different state equations may be used for density or viscosity [1].

195 3. The numerical model

196 The system of nonlinear equations (1)–(7), valid in 3D domains, is solved hereafter for 2D
197 vertical domains using adapted advanced numerical methods that allow an accurate estimation
198 of the velocity and concentration distributions for heterogeneous domains and unstructured
199 meshes. The main stages to form the final system to be solved are summarized hereafter for a
200 general triangular mesh.

201 *3.1 The lumped MHFE method for modeling fluid flow*

202 With the classical standard FE method, the head is approximated linearly inside each element
203 using standard chapeau functions, and hence, the velocity is constant at the element level.
204 With the MHFE method, we assume a linear approximation for the velocity $\boldsymbol{q}$ inside each
205 triangle E using the linear Raviart-Thomas basis functions:

206 $$\boldsymbol{q} = \sum_{j=1}^{3} Q_j^E \boldsymbol{w}_j^E \quad (8)$$

207 where Q_j^E is the flux across the edge j of E and $\boldsymbol{w}_j^E$ is the Raviart-Thomas basis function
208 [41].

209 The mass lumping procedure is used to avoid over- and undershoots observed for transient
210 simulations with small time steps [27, 28]. The basic idea of this procedure is to consider

steady-state flow (the mean head at the element E is $H_E = \left(TH_1^E + TH_2^E + TH_3^E\right)/3$), and then the transient component is directly added to the expression of the flux [35]:

$$Q_i^E = \sum_j N_{ij}^E \left(TH_j^E + \frac{\rho_E - \rho_0}{\rho_0} z_j^E \right) - \frac{|E|}{3} r_E \frac{dTH_i^E}{dt} + \frac{Q_S^E}{3} \tag{9}$$

where TH_i^E (resp. z_i^E) is the mean head (resp. mean elevation) of the edge i of E with $TH_i = Th_i + z_i$, Th_i is the mean pressure head, j is an edge of E, N is a local matrix of coefficients $N_{ij}^E = -k_r^E \frac{det\left(\boldsymbol{K}_E\right)}{|E|} \boldsymbol{r}_i^T . \boldsymbol{K}_E^{-1} . \boldsymbol{r}_j$ where $\boldsymbol{r}_i$ is the edge vector face to the vertex i of the element E (see Younes *et al.* [42] for more details), $|E|$ is the area of E, $r_E = c\left(h_E\right) + S_S\, \theta\left(h_E\right)/\theta_S$ is the accumulation term in Richards' equation, h_E is the mean pressure head at E, and $Q_S^E = \int_E q_S$ is the sink term on E.

The final flow system is formed by imposing continuity of heads $\left(TH_i^E = TH_i^{E'}\right)$ and fluxes $\left(Q_i^E + Q_i^{E'} = 0\right)$ between the adjacent elements *E* and *E'* having a common edge i:

$$\sum_j N_{ij}^E \left(TH_j^E + \frac{\rho_E - \rho_0}{\rho_0} z_j^E \right) + \sum_j N_{ij}^{E'} \left(TH_j^{E'} + \frac{\rho_{E'} - \rho_0}{\rho_0} z_j^{E'} \right) - \left(\frac{|E|}{3} r_E + \frac{|E'|}{3} r_{E'} \right) \frac{dTH_i^E}{dt} + \frac{Q_S^E}{3} + \frac{Q_S^{E'}}{3} = 0 \tag{10}$$

The indices i and j are global, and the system is solved for the mean heads at edges TH_i.

In the case of a Dirichlet condition with a prescribed head H_{imp} at the boundary edge *i*, equation (10) is replaced by $TH_i = H_{imp}$. If the boundary edge *i* has a prescribed flux Q_{imp} (Neumann boundary condition), equation (10) is replaced by $Q_i^E + Q_{imp} = 0$.

Note that the system of equations (10) is highly nonlinear since (*i*) the local matrix N and the accumulation term r depend on the pressure head and (*ii*) the hydraulic conductivity and the buoyancy term depend on the concentration.

3.2 The DG-MPFA method for modeling solute transport

Using the mass conservation of the fluid, given by equation (1), the transport equation (3) simplifies to:

$$\theta \frac{\partial C}{\partial t} + \boldsymbol{q} \nabla C + \nabla . \boldsymbol{q}_D = 0 . \tag{11}$$

With $\boldsymbol{q}_D = -\boldsymbol{D} \nabla C$, the dispersive flux, assumed to have a constant divergence over the element *E*:

$$\nabla . \boldsymbol{q}_D = \frac{1}{|E|} \sum_i Qd_i^E \tag{12}$$

where Qd_i^E is the dispersive flux across the edge *i* of E.

The concentration inside the element *E* is approximated with linear discontinuous functions:

$$C^E = \sum_{i=1}^{3} C_{E,i} \phi_{E,i} \tag{13}$$

with $\phi_{E,i}$ being the interpolation function and *i* a local index that refers to the i^{th} DOF $C_{E,i}$ of the concentration inside the element *E*.

In the literature, the DOFs are often chosen (see, for instance, [43]) to be the concentration at the nodes and $\phi_{E,i}$, the classical chapeau functions. In this work, the DOFs are the mean

concentration $C_{E,1}$ and the components of the concentration gradient $C_{E,2}$ and $C_{E,3}$, with the corresponding interpolation functions:

$$\phi_{E,1}=1, \qquad \phi_{E,2}=\left(x-x_E\right), \qquad \phi_{E,3}=\left(z-z_E\right),$$

where x and z are horizontal and vertical coordinates, and x_E and z_E are the coordinates of the center of the element E. Thus, the polynomial approximation of the concentration inside the element E is $C^E=C_{E,1}+C_{E,2}\left(x-x_E\right)+C_{E,3}\left(z-z_E\right)$.

The variational formulation of Eq (11) using the test function $\phi_{E,i}$ is:

$$\int_E \theta\frac{\partial C}{\partial t}\phi_{E,i}-\int_E C\nabla.\left(\boldsymbol{q}\phi_{E,i}\right)+\int_E \nabla.\left(\boldsymbol{q}C\,\phi_{E,i}\right)+\int_E \phi_{E,i}\nabla.\boldsymbol{q}_D=0\,. \tag{14}$$

Using Green's formula and Eq (12) and Eq (13), we obtain:

$$\sum_j \frac{dC_{E,j}}{dt}\theta_E\int_E \phi_{E,j}\phi_{E,i}-\sum_j\int_E C_{E,j}\phi_{E,j}\,\nabla.\left(\boldsymbol{q}\phi_{E,i}\right)+\sum_j\int_j C_j^*\phi_{E,i}\,\boldsymbol{q}.\boldsymbol{\eta}_j^E+\sum_j Qd_j^E\int_E \phi_{E,i}=0 \tag{15}$$

where C_j^* is the upstream concentration at the edge j, $\boldsymbol{\eta}_j^E$ is the unit outward normal vector to the edge j of E, and $\boldsymbol{q}$ is the velocity obtained by substituting equation (9) into equation (8).

Equation (15) is written for the three test functions $\phi_{E,i}$ $\left(i=1,2,3\right)$ for each element E. The index j $\left(j=1,2,3\right)$ refers to the j^{th} DOF of the concentration in the element E in the two first terms of Eq (15) and to the j^{th} edge of E for the last two terms in equation (15).

The upstream concentration C_j^* at the edge j can be written as follows:

262 $$C_j^* = \tau_j^E C_j^E + \left(1-\tau_j^E\right) C_j^{E'} \tag{16}$$

263 with $\tau_j^E = 1$ for an outward flux $\left(\boldsymbol{q}.\boldsymbol{\eta}_j^E \geq 0\right)$, else $\tau_j^E = 0$.

264 Thus, C_j^* corresponds to C_j^E, the concentration at the edge j calculated using the polynomial
265 approximation of the concentration at the element E, or $C_j^{E'}$, the concentration at j
266 calculated using the polynomial approximation of the concentration at the element *E'*, sharing
267 the edge j with E.

268 Equation (15) yields three equations for each element E having 3 adjacent elements
269 $\left(E1, E2, E3\right)$:

270 $$[A]\begin{pmatrix} \frac{dC_{E,1}}{dt} \\ \frac{dC_{E,2}}{dt} \\ \frac{dC_{E,3}}{dt} \end{pmatrix} = [B]\begin{bmatrix} C_{E,1} \\ C_{E,2} \\ C_{E,3} \end{bmatrix} - \left[M^0\right]\begin{bmatrix} C_{E,1} \\ C_{E,2} \\ C_{E,3} \end{bmatrix} - \sum_{\ell=1}^{3}\left[M^\ell\right]\begin{bmatrix} C_{E\ell,1} \\ C_{E\ell,2} \\ C_{E\ell,3} \end{bmatrix} - \begin{bmatrix} \sum_j Qd_j^E \\ 0 \\ 0 \end{bmatrix} \tag{17}$$

271 with:

272 $$A_{i,j} = \theta_E \int_E \phi_{E,j}\phi_{E,i} \qquad B_{i,j} = \int_E \phi_{E,j}\,\nabla.\left(\boldsymbol{q}\phi_{E,i}\right)$$
$$M_{i,j}^0 = \sum_\ell \tau_\ell^E \boldsymbol{q}.\boldsymbol{\eta}_\ell^E \int_\ell \phi_{E,i}\,\phi_{E,j} \qquad M_{i,j}^\ell = \left(1-\tau_\ell^E\right)\boldsymbol{q}.\boldsymbol{\eta}_\ell^E \int_\ell \phi_{E,i}\,\phi_{E\ell,j}$$

273 To avoid operator splitting between advection and dispersion, the dispersive flux Qd_j^E in
274 equation (17) is approximated using the MPFA method. The latter has similar properties to
275 the MFE method since both are locally conservative and can handle unstructured meshes and
276 anisotropic and heterogeneous domains. The two methods can be equivalent for some specific
277 situations [34, 44]. However, contrary to the MHFE method, which uses the concentration at

278 the edges as DOFs, MPFA uses the mean concentration at each element as DOFs. Hence, the
279 discrete approximation of Qd_j^E can be directly added to the system of equations (17), which
280 avoids the necessary operator splitting if the MHFE method is used for dispersion, as in [30].

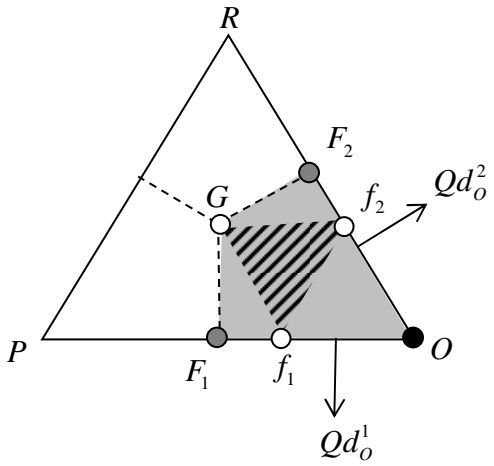

281

282 **Figure 1.** A triangular element divided into three subcells, with linear concentration
283 approximation on each subcell.

284 To calculate Qd_j^E with the MPFA method, we assume that the concentration inside the sub-
285 cell (O, F_1, G, F_2) formed by the node O, the center G, and the mid-edges F_1 and F_2 (gray
286 area in the Figure 1) is linear. Hence, it can be approximated using $C_{E,1}$, λ_1 and λ_2 the
287 concentrations at respectively G and the two continuity points f_1 and f_2 located at

288 $$\frac{Of_1}{OF_1} = \frac{Of_2}{OF_2} = \frac{2}{3}.$$

289 Therefore, (O, f_1, G, f_2) is a parallelogram, and the half-edge fluxes

290 $$\left(Qd_O^1 = \int_O^{F_1} -\boldsymbol{D}\nabla C \text{ and } Qd_O^2 = \int_O^{F_2} -\boldsymbol{D}\nabla C \right) \text{ are}$$

291 $$\begin{pmatrix} Qd_O^1 \\ Qd_O^2 \end{pmatrix} = \frac{3}{|E|} \begin{pmatrix} -\overrightarrow{OF_1}^{\perp}.\boldsymbol{D_E}.\overrightarrow{OF_1}^{\perp} & \overrightarrow{OF_1}^{\perp}.\boldsymbol{D_E}.\overrightarrow{OF_2}^{\perp} \\ \overrightarrow{OF_1}^{\perp}.\boldsymbol{D_E}.\overrightarrow{OF_2}^{\perp} & -\overrightarrow{OF_2}^{\perp}.\boldsymbol{D_E}.\overrightarrow{OF_2}^{\perp} \end{pmatrix} \begin{pmatrix} \lambda_1 - C_{E,1} \\ \lambda_2 - C_{E,1} \end{pmatrix} \quad (18)$$

where $\boldsymbol{D}_E$ is the dispersion tensor of the element E, given by equation (4) and using the velocity at the center of E from equations (8) and (9).

Equation (18) is written for all elements sharing the vertex O. Then, imposing continuity of half-edge fluxes and continuity of the concentration at the continuity points gives a local system, which we invert to obtain explicitly the concentration at each continuity point as a function of the concentration at all elements sharing the node O. The latter is then replaced in equation (18), and the summation of all half-edge fluxes is then substituted into equation (17) (see [29] for more details). Therefore, the first line of the system (17) contains the contribution of all elements sharing at least one node of the element E. The second and third equations of (17) contain the contribution of adjacent elements sharing an edge with E. Note that, because of the judicious choice of DOFs, the DG_MPFA scheme reduces to an upwind FV_MPFA scheme by removing the second and third equations of (17) for all mesh elements.

The final vector of residuals for the global flow-transport nonlinear system is formed by the system of equations (10), written for the unknown pressure head TH_i at the edges, followed by the system of equations (17), written for the three unknown DOFs of the concentration at each element.

3.3 The temporal discretization

The coupled nonlinear flow equation (10) and transport equation (17) are written in a single implicit system of ordinary differential equations (ODEs) or differential algebraic equations (DAEs) of the general form:

$$F\left(t, \boldsymbol{y}, \boldsymbol{y}'\right) = 0 \tag{19}$$

where $\boldsymbol{y} = \left[\left(TH_i\right)_{i=1,..,nb\_edges}, \left(C_{E,1}, C_{E,2}, C_{E,3}\right)_{E=1,..,nb\_elements} \right]$ is the vector of unknowns formed

by (*i*) the head traces at all the edges of the mesh (except Dirichlet boundary edges) and (*ii*) the three DOFs for the concentration at each element of the mesh. This vector reduces to $\boldsymbol{y} = \left[\left(TH_i \right)_{i=1,..,nb\_edges}, \left(C_{E,1} \right)_{E=1,..,nb\_elements} \right]$ with only one DOF per element for the concentration in the case of FV (instead of DG) formulation.

The system (19) is solved in time using higher-order methods, which are known to be more efficient than lowest-order methods. Indeed, higher-order methods allow larger time steps and less effort in the nonlinear solver compared with the lowest-order methods [45]. Furthermore, higher-order methods are often combined with an efficient automatic time-stepping scheme, which improves the computational efficiency. The time-step size management is optimized to maintain a given temporal discretization error [36, 45-47].

Among the integration methods, the Backward Difference Formula (BDF) has good stability properties and is well adapted for time integration of stiff problems [48]. The Fixed Leading Coefficient Backward Difference Formula (FLCBDF) is used in this work via the DASPK solver. The basic idea of the k^{th}-order FLCBDF method is to convert the system $F\left(t_n, \boldsymbol{y}_n, \boldsymbol{y}'_n\right) = 0$ at a given time $t_n = t_{n-1} + \underline{h}$ with solution history $\boldsymbol{y}_{n-1}, ..., \boldsymbol{y}_{n-k}$ to the system $F\left(t_n, \boldsymbol{y}_n, \hat{a}\boldsymbol{y}_n + \hat{\boldsymbol{b}}\right) = 0$ where $\hat{a}$ and $\hat{\boldsymbol{b}}$ depend on the step size $\underline{h}$, the order k, and the solution history (see [49] for more details).

The main advantages of the FLCBDF method are: (*i*) it avoids the unstable behavior of the interpolated fixed-step methods and (*ii*) the Newton iteration matrix can be reused for more steps than in a fully variable-step approach [38, 50].

The Jacobian matrix is evaluated numerically using finite difference approximation. The same Jacobian matrix is used for several time steps to improve efficiency. Furthermore, to reduce drastically the computational time required for the calculation of the Jacobian, sparsity and

structure of $\boldsymbol{J}$ are provided and the variables are perturbed by group using the column grouping technique (see [51, 52]).

The order (up to the fifth-order) of BDF, as well as the time step's size, are optimized to reduce the computational effort while maintaining a small temporal truncation error. The latter is estimated using a predictor-corrector scheme. Both absolute and relative convergence criteria are fixed to 10^{-5} in this work.

In this work, we use the DASPK time solver with the preconditioned Krylov iterative method to solve the linear systems arising at each time step.

4. Numerical experiments

Three test cases are investigated to show the efficiency and accuracy of the developed numerical model. The first test case is inspired by the laboratory experiment performed by Vauclin *et al.* [53]. It deals with the infiltration, under constant flux, of a dense contaminant into an unsaturated-saturated porous medium. This test, which is relatively simple from a computational point of view, is used to validate the developed code against a standard finite element solution obtained using COMSOL Multiphysics®. The second test case, inspired by the work of Forsyth and Kropinski [54], deals with the infiltration of a dense contaminant in a heterogeneous initially dry soil. The simulated moving sharp front induces high nonlinearity, which makes this computational test cases very challenging. It is used to highlight the efficiency of our newly developed model and to assess the advantages of combining high-performance numerical methods compared with classical ones implemented in COMSOL. The last test case is investigated to show the applicability of the new model to large-scale problems. In this test case, the developed numerical tool is used to simulate a simplified conceptual 2D model of saltwater intrusion under climate change for the Akkar coastal aquifer in Lebanon.

4.1 Infiltration of a dense contaminant in an unsaturated-saturated porous medium

Vauclin *et al.* [53] performed laboratory experiments to investigate the transient position of the water table under artificial recharge. The problem is extended here by including the infiltration from the surface of a dense contaminant and used for the validation of the new model by comparison with COMSOL results. The domain is a rectangular sandbox of 600 cm × 200 cm, with the water table located at 65 cm from the bottom. The initial conditions correspond to hydrostatic pressure distribution with a domain free from pollutants. Infiltration of a contaminant under a constant flux of 86.4 cm/day is then applied over 200 cm in the center of the soil surface. A Dirichlet boundary condition with a head of 65 cm is fixed below the water table. A no-flow boundary is prescribed for the bottom and top surface, except for the infiltration zone. Owing to the symmetry of this problem, only the right-hand side of the domain is modeled with a no-flow boundary imposed along the axis of symmetry. The material properties are given in Table 1.

Table 1. Simulation parameters for the first test case inspired from Vauclin *et al.* [53].

Parameters	
θ_r	0.01

θ_s	0.3
$\alpha(cm^{-1})$	0.033
n	4.1
$K\left(cm.s^{-1}\right)$	10^{-2}
$S_s\left(cm^{-1}\right)$	10^{-10}
$\alpha_L\left(cm\right)$	1
$\alpha_T\left(cm\right)$	0.1
$D_m\left(m^2/s\right)$	10^{-9}
$\rho_0\left(kg/m^3\right)$	1000
$\rho_1\left(kg/m^3\right)$	1000 or 1100
$\mu\left(kgm^{-1}s^{-1}\right)$	0.001

The simulation is performed for 80 hours using a triangular mesh formed by 4273 triangular elements. Two configurations are investigated: in the first one, the injected contaminant is a tracer $\left(\rho_1 = 1000\,kg/m^3\right)$, whereas in the second, the contaminant has a higher density $\left(\rho_1 = 1100\,kg/m^3\right)$.

The evolution of the contaminant plume during the time for both situations is shown in Figure 2. Before reaching the water table (initially at $z = 65$ cm), the tracer and dense contaminant plumes are almost the same (see results at $t = 15$ h). Indeed, density variation seems to have no effect during the transport through the unsaturated zone. The main reasons for this similarity are that (*i*) a fixed flux is used at the surface and hence the same quantity of contaminant is intruded in the system for both situations and (*ii*) the density variation in the liquid phase (10%) is much less important than the density variation between the liquid and air phase, which is about three orders of magnitude. This last reason is no longer valid once the plume reaches the water table. As a consequence, due to density effects, the dense contaminant moves downward in the saturated domain, creating a recirculation zone (vortex) near the water table interface (see results of Figure 2, at $t = 30$ h), whereas the tracer

contaminant remains near the water table. The velocity distribution in the unsaturated zone is quite similar for the tracer and dense contaminant situations, whereas strong differences can be observed in the saturated zone. For the tracer contamination, the velocity is not affected by the evolution of the contaminant and remains mainly horizontal. However, in the case of the dense contaminant, strong vertical velocities appear due to density effects, which bring the contaminant down to the bottom. As a consequence, the results in terms of velocity field and contaminant distribution at $t = 80$ h for the dense and tracer situations are completely different. The tracer moves mainly horizontally at the upper part of the saturated zone with a maximum displacement near the water table, whereas the dense contaminant moves toward the substratum and then horizontally in the lower part of the domain. The vortex remains near the water table interface (see results of Figure 2 at $t = 80$ h).

The validity of the new model is investigated by comparing the obtained results against those of the popular COMSOL model. The same spatial discretization was used to allow for a comparison between COMSOL and our newly developed model, and the solution was also checked on a fine mesh since no analytical solution is available. The results of the two models are almost similar, which demonstrates the validity of the developed model (Figure 3). Notice that the non-dimensional mass injected from the upper boundary during the simulation is 0.288. With the new numerical model, the total mass in the domain at 80h is 0.28815, whereas it is 0.2820 with COMSOL. Hence, the mass balance error with COMSOL is around 0.021, whereas it is around 5×10^{-4} with the new model. Therefore, the very small difference observed in Figure 3 between the isocontour levels of the new model and COMSOL is probably due to the loss of mass observed with COMSOL.

Both COMSOL and the new model were used with the MOL and a variable high-order (up to 5) time integration BDF method. The evolution of the time step's length with the new model during the simulation of the tracer and the dense contaminant infiltration situations are

depicted in Figure 4. The tracer simulation required 51s of CPU time, for a total number of 1128 time steps. The time step starts at 10^{-4} s and increases to 1655 s in almost a monotonic way (see Figure 4a). Only 37 Jacobian evaluations are required during the 1128 time steps. The simulation of the dense contaminant required more CPU time (70 s) and needed more time steps (1751). In this case, smaller time steps are used (the maximum is 389 s), and the time step size is no longer monotonic (Figure 4b), probably because of the more complex occurring physics. Note that the evolution of the time step's size remains quite similar before the wetting front reaches the saturated zone. The same Jacobian is maintained for several time steps since the number of evaluations of the Jacobian remains small (only 40 evaluations), which shows the efficiency of the new model.

As a comparison, the simulation of the dense contaminant with COMSOL requires 1452 time steps. The evolutions of the time step's length with both models are similar. However, the new model was around 10 times more efficient than COMSOL. Indeed, the new model spent only 70 seconds of CPU time, whereas COMSOL required 720 seconds for the whole simulation. In fact, COMSOL was very slow in the early stages of simulation, probably due to the significant oscillating pressure and concentration values observed in the neighborhood of the infiltration front. These unphysical oscillations affect the convergence of the nonlinear solver and increase the number of nonlinear iterations per time step.

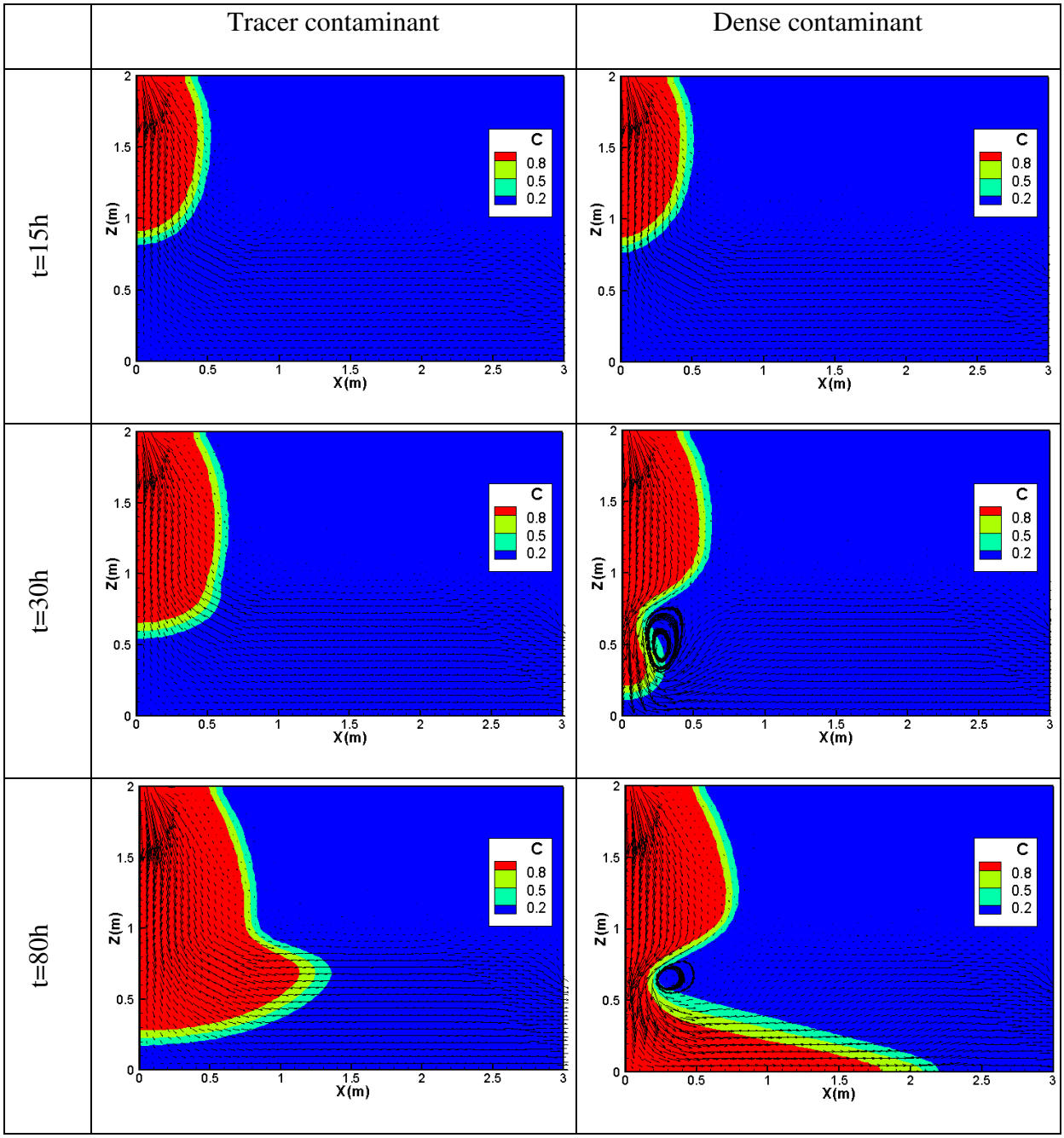

444

445 **Figure 2.** velocity field and contaminant distributions for the infiltration of a tracer and a
446 dense contaminant in an unsaturated-saturated system.
447

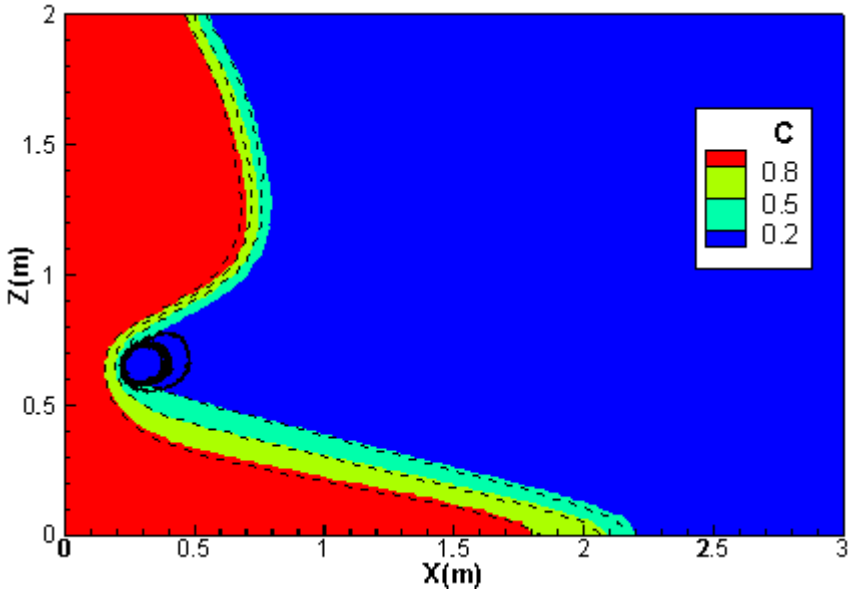

448
449 **Figure 3.** Concentration distribution at t = 80h for the dense contaminant infiltration: Results
450 of the new model (contours) versus COMSOL results (dashed-lines)

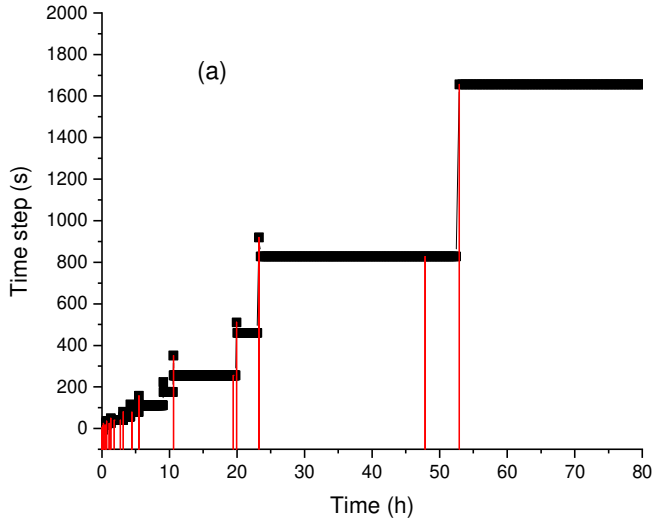

451

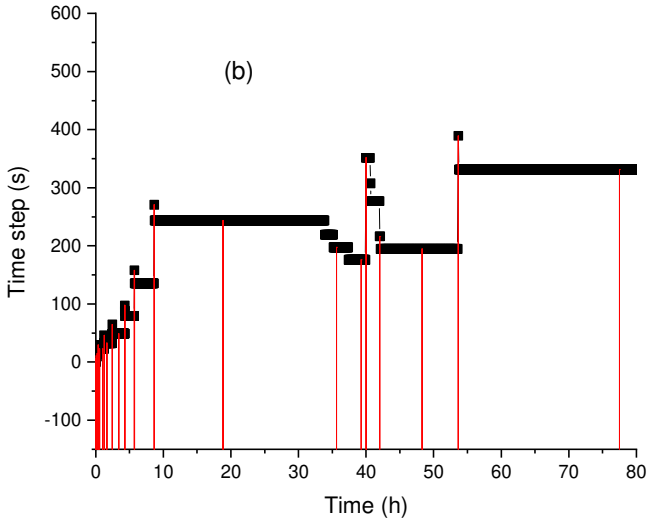

452
453 **Figure 4.** Time step evolution for the tracer (a) and dense (b) contaminant infiltration
454 simulated with the new model.

4.2 Infiltration of a dense contaminant in a heterogeneous initially dry soil

Simulating infiltration into dry soils is known to be a challenging task. Indeed, for very dry conditions, the head gradient becomes extremely large at the wetting front, which can lead to large computational times and unphysical oscillations [20]. To investigate the efficiency of the developed model for such situations, we simulate the infiltration problem given in [36]. The problem is inspired from Huang *et al.* [55] and involves infiltration under a constant head boundary condition into a heterogeneous dry soil. The domain has a rectangular shape of 125 cm width and 230 cm depth and contains two horizontal layers. The surface layer of 40 cm thickness is formed by a clayey soil. The subsurface layer is a sandy soil of 190 cm thickness. The properties of the two soil layers are depicted in Table 2. A Dirichlet boundary condition is prescribed in the strip $0 \le x \le 20\,\text{cm}$ at the surface with a fixed pressure head of -10 cm. A fixed pressure head of -10^4 cm is maintained at the bottom of the domain. The other sides are impervious. A constant initial pressure head of -10^4 cm is considered for the entire domain, which corresponds to an initial water content of 0.059 $\text{cm}^3.\text{cm}^{-3}$ and 0.045 $\text{cm}^3.\text{cm}^{-3}$, respectively, in the upper and lower layer. The infiltrated contaminant has a density of 1025kg.m^{-3}, which corresponds to seawater density. A triangular mesh of 3505 elements is used for the spatial discretization, and the final simulation time is 7 days.

Table 2. Simulation parameters for the problem of contaminant infiltration in a heterogeneous initial dry soil.

Parameters	Upper Layer	Lower Layer
θ_r	0.0001	0.045
θ_s	0.40	0.43
$\alpha(cm^{-1})$	0.0174	0.145
n	1.37	2.68
$K\left(\times 10^{-4}\, cm.s^{-1}\right)$	3.5	82.5
$S_s\left(\times 10^{-10}\, cm^{-1}\right)$	1	1
$\alpha_L\left(cm\right)$	0.5	0.5
$\alpha_T\left(cm\right)$	0.1	0.1
$D_m\left(m^2/s\right)$	10^{-9}	10^{-9}
$\rho_0\left(kg/m^3\right)$	1000	1000
$\rho_1\left(kg/m^3\right)$	1025	1025
$\mu\left(kgm^{-1}s^{-1}\right)$	0.001	0.001

The obtained pressure and concentration distributions are shown in Figure 5. In this figure, the pressure shows a sharp front, reflecting a very high gradient caused by the dry initial conditions (-100 m).

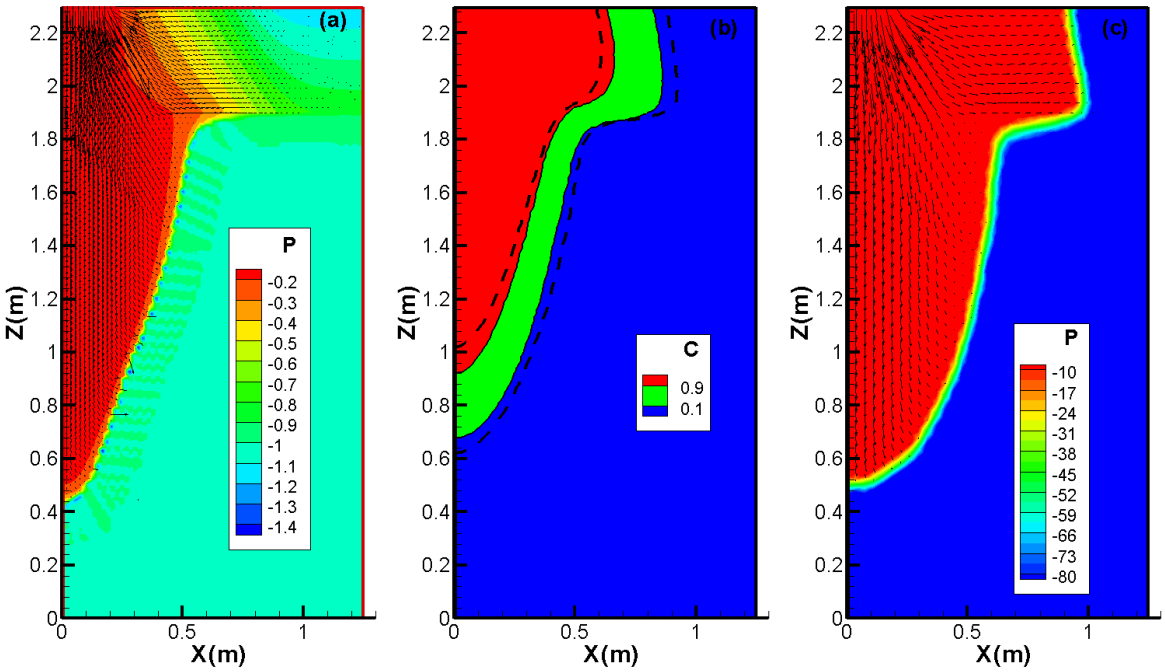

Figure 5. (a) Pressure distribution (in m) with COMSOL, (b) pressure and (c) concentration distributions with the new model at t = 7 days for the problem of contaminant infiltration in a heterogeneous initial dry soil. Dashed lines represent results of upwind first order FV instead of DG for advection.

The sharp pressure front cannot be accurately simulated with COMSOL. Indeed, the simulation of this test case with COMSOL using the same mesh failed to converge because of unphysical oscillations generated near the wetting interface. Convergence problems have been also encountered when changing the initial (and bottom) conditions from -100 m to -1 m. The only way to obtain a convergent solution with COMSOL was to use a finer mesh of about 14,000 elements and an initial pressure head of -1 m instead of -100 m. And, even for such a situation, the results of COMSOL are inaccurate since the obtained pressure head is between -1.4 m and -0.1 m instead of -1 m and -0.1 m. Besides, the solution contains strong unphysical oscillations near the wetting interface (Figure 5a). These unphysical oscillations are avoided with the new code, thanks to the used advanced numerical methods and, especially, the mass lumping procedure, which avoids unphysical oscillations in the case of transient simulations with sharp wetting fronts [27, 28].

Figure 5c shows the final concentration distribution at t = 7 days. The results of a simplified version of the numerical code using the upwind first-order FV scheme instead of DG are also depicted (dashed lines) in Figure 5c. This figure shows that a large numerical diffusion is generated using the upwind first-order FV method. To quantify the difference between the two methods, the spread of the concentration $L_S = X_{0.9} - X_{0.1}$, corresponding to the distance between the 10% and 90% isochlors at the left vertical side of the domain, is measured for the FV and DG simulations. The spread with FV is $L_S^{FV} = 0.4$, whereas with DG, it is $L_S^{DG} = 0.24$. Hence, due to numerical diffusion, the spread with the FV method is around 170% that of DG. This shows clearly that DG is well-adapted for advective-dominated transport and generates limited numerical diffusion compared with the upwind first-order FV method.

It is worth noting that, in the first test case, the contaminant distribution in the unsaturated

512 region was not affected by the density of the contaminant, since the infiltration occurred under
513 a constant flux boundary condition. For the current test case, the concentration distribution is
514 sensitive to the density of the contaminant because of the Dirichlet boundary condition used at
515 the surface infiltration boundary (results are not shown in the paper). The pollutant infiltration
516 is slightly more pronounced with the dense contaminant than with the tracer contaminant. The
517 total mass in the system at t = 7 days is 0.64 kg with the tracer, whereas it is 0.66 kg if the
518 contaminant has a density of 1025 kg.m^{-3}. This total mass can increase up to 0.76 kg in the
519 case of a contaminant with a density of 1200 kg.m^{-3} (brine contamination).

520 Finally, to highlight the benefit of the higher-order time integration for the investigated
521 challenging infiltration problem, we compare the efficiency of the model when used with a
522 first-order and with a variable high-order (up to 5) time integration with the BDF method.

523 **Table 3.** Performance statistics for the first-order and variable order methods implemented in
524 the advanced developed model for the simulation of the second test case.

Time integration method	CPU	Nb time steps	Nb Jacobian	Max time step	Mean time step
First-order	896	28871	115	45	21
Variable-order (up to 5)	128	4322	138	378	140

525

526 The results of Table 3 show that the high-order method requires more Jacobian evaluations,
527 but allows much larger time steps and needs fewer calculations compared with the classical
528 first-order method. The variable high-order method is around 7 times more efficient than the
529 first-order method for the investigated problem.

530 *4.3 Large-scale simulation of SWI under climate change*

531 The developed numerical tool is used to simulate a large-scale contamination problem with
532 large spatial and temporal ranges that occurs in the Akkar unconfined coastal aquifer, located

533 in the north of Lebanon (Figure 6a). The plain is cultivated with market gardening and cereals
534 crops and the aquifer underwent a significant increase in pumping water, both for irrigation
535 and domestic consumption, notably because of the massive arrival of Syrian refugees in the
536 region. As a consequence, some pumping wells suffer from salinization caused by the
537 overexploitation of the aquifer.

538 Because of the lack of data (infiltration rates, piezometric heads, etc) and of precise
539 knowledge of initial and boundary conditions, a full 3D simulation of the above-described
540 problem has not been considered. A representative 2D vertical cross-section is designed to
541 investigate saltwater intrusion under climate change projection and long-term pumping
542 regimes.

543

544

545

546

547

548

549

550

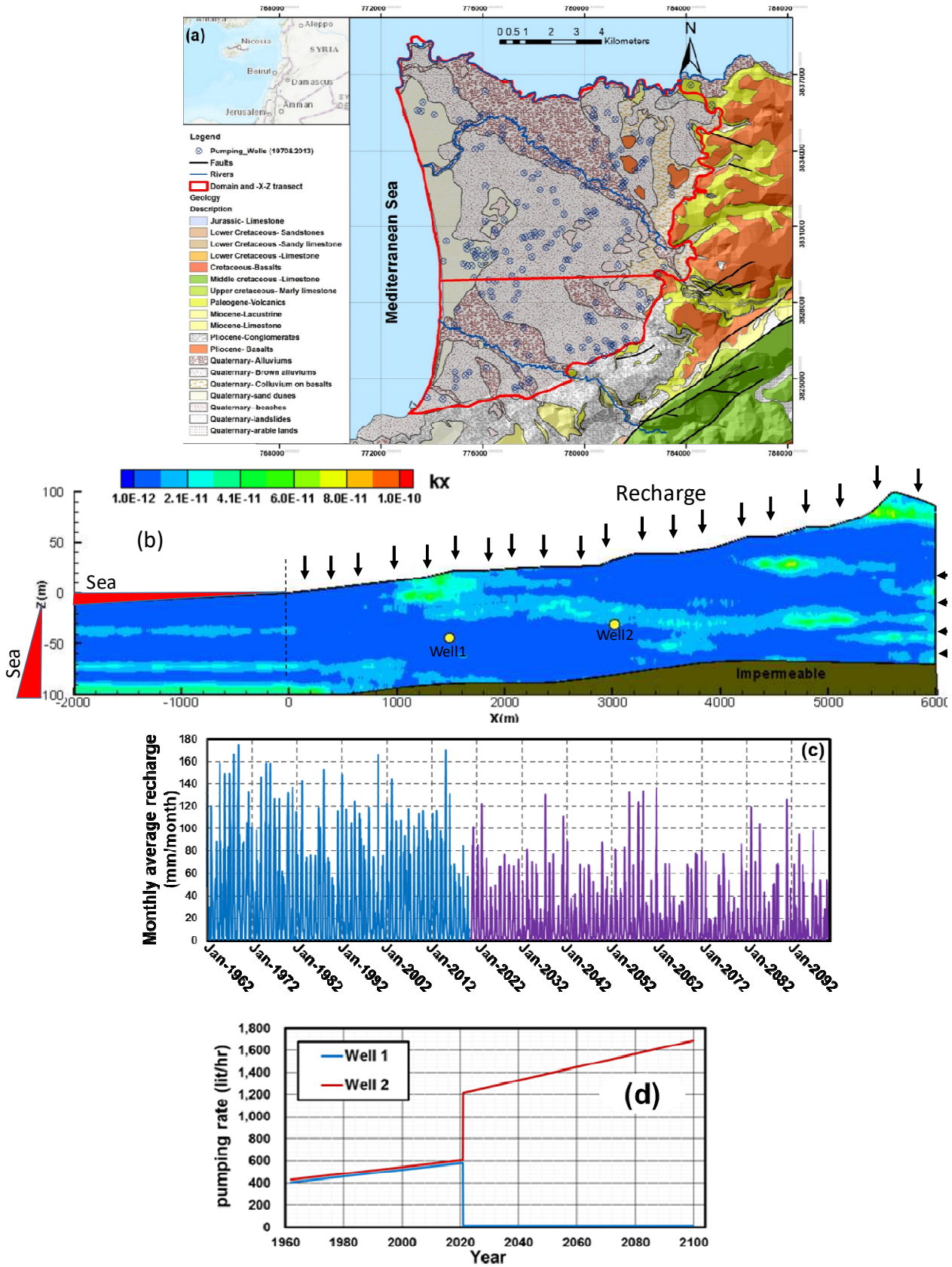

551 **Figure 6.** (a) Location of the Akkar aquifer, (b) conceptual representation of the aquifer with
552 a lognormal permeability field and the boundary conditions (c) the recharge data until 2019
553 and projections under climate change between 2020 and 2099 and (d) pumping rates in
554 production wells.

555 The shore-perpendicular section has an extension of 2 km offshore and 6 km onshore [56].
556 The depth of the Akkar basin varies between 100 m and 170 m from the surface and is formed
557 by fluvial deposits. In the conceptual model (Figure 6b), the permeability field was generated
558 assuming a lognormal distribution with a variance of 1.0 m^4 and a geometric average
559 conductivity of 0.945 10^{-11} m^2. An exponential correlation function was used with horizontal
560 and vertical correlation lengths of 1000 m and 10 m, respectively. The bottom is formed by
561 clays and marls and is considered impermeable. The left vertical side corresponds to the sea
562 boundary, which has a prescribed concentration of C = 35 $g.l^{-1}$ and a vertical hydrostatic
563 pressure distribution. The recharge, depicted in Figure 6c, corresponds to observed data for
564 the period between 1962 and 2020 and a projection for the period 2020–2099, obtained from
565 the IPSL_CM5 Global Climate Model (GCM) [57]. A weak regional flow is assumed at the
566 right land boundary. Although radial upconing around wells have necessarily 3D
567 configurations, two wells are assumed to represent the different pumping activities in the
568 Akkar aquifer [58]. The wells are located at, respectively, 1500 m and 3000 m from the
569 shoreline at, respectively, a depth of 45 m and 30 m. The rates for the two pumping wells
570 (Figure 6d) are assumed to represent the observed rates for the period 1962–2020 and
571 expected rates (with increasing water demand) for 2020–2099. Note that pumping was
572 stopped for Well 1 (the closest to the sea) in 2020 because of salinization. The pumping rate
573 of Well 1 was transferred to Well 2.

574

575

576

577

578

579 **Table 4**. Properties of the soil and the water for the simulation of the simplified conceptual
580 Akkar aquifer.

Parameter	Value
Freshwater density $\rho_0\left(kg.m^{-3}\right)$	1,000
Seawater density $\rho_1\left(kg.m^{-3}\right)$	1,025
Gravity $g(m.s^{-2})$	9.81
Viscosity $\mu(kg.m^{-1}.s^{-1})$	10^{-3}
Anisotropy ratio $r_k(=k_z/k_x)$	0.1
Porosity ε	0.39
Storage coefficient $S_s(m^{-1})$	5×10^{-4}
Molecular diffusion $D_m(m^2.s^{-1})$	1.0×10^{-9}
$\alpha(cm^{-1})$	0.01
n	1.75
θ_s	0.39
θ_r	0.1
$\alpha_L\left(m\right)$	5
$\alpha_T\left(m\right)$	0.5
Right boundary condition: Regional flow/ unit width $q_d(m^2.s^{-1})$	6×10^{-7}

581

582 The domain is discretized with approximately 75K triangular elements with an almost equal
583 area of 15 m^2. The simulation is, at first, performed for a long time with the yearly average
584 recharge of pre-1962, without pumping to mimic the natural equilibrium conditions (Figure
585 7a). The value of recharge for this period is taken uniformly and equal to 90 $mm.y^{-1}$. Next,
586 two periods are simulated: (*i*) the 1962–2020 period, which leads to the current situation of
587 the coastal aquifer (Figure 7b), and (*ii*) the 2020–2099 period, which corresponds to the future
588 response of the aquifer to the impact of a climate change projection and estimated pumping
589 regime (Figure 7c).

590 The problem is solved for 333,031 DOFs (unknowns) on a computer with a single Intel i7-
591 7700 processor 3.6 GHz and 16 Go of RAM (i.e. Random Access Memory). The whole
592 simulation (138 years) required around 9h of CPU time.

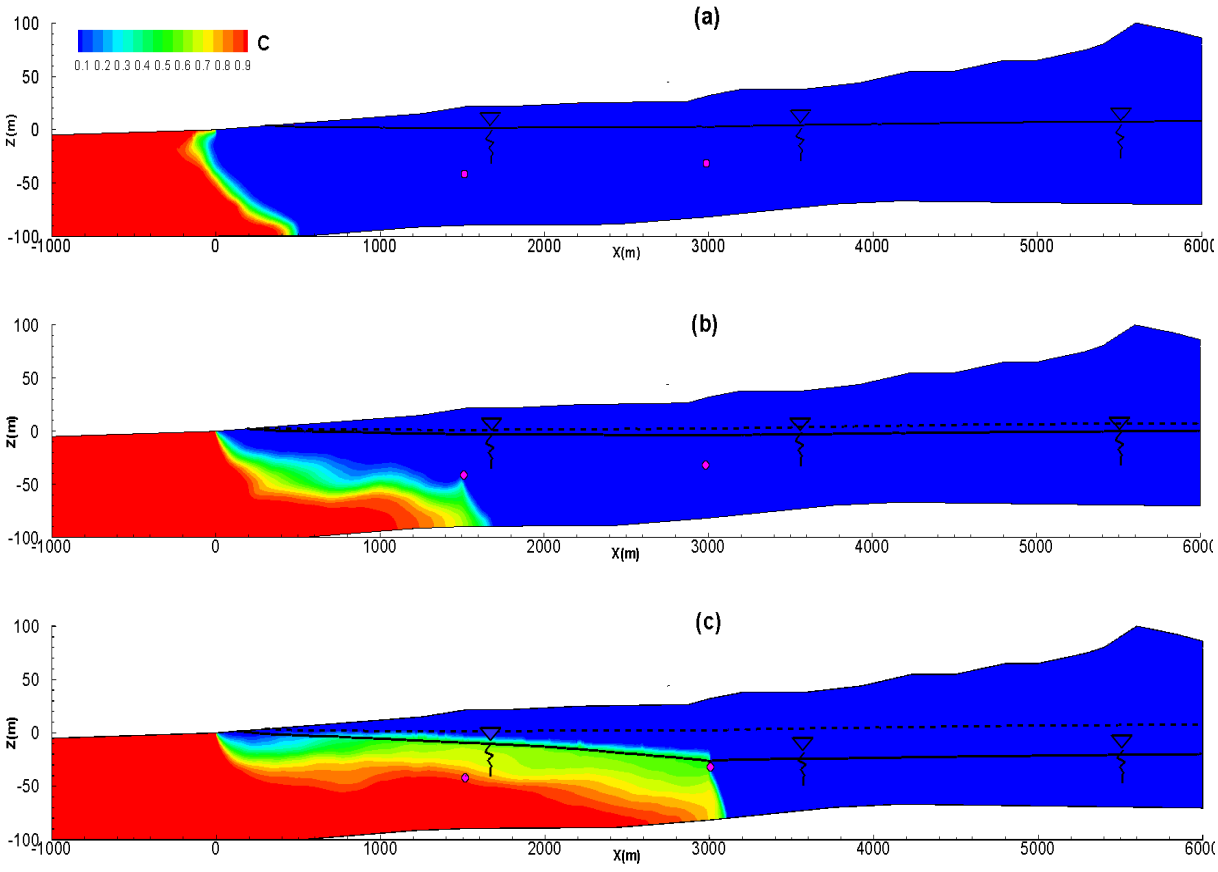

Figure 7. Spatial salinity distribution in the aquifer and water table position: (a) at 1962 (state of equilibrium), (b) currently at 2020 and (c) predictions for 2099.

Figure 7a shows that, without any pumping, the natural equilibrium situation of 1962 shows a moderate saltwater intrusion. The concentration profile shows a small dispersion. The aquifer is only contaminated near the bottom, for a distance of around 400 m from the shoreline. Because of pumping, the concentration distribution at 2020 shows a more significant saltwater intrusion. In Figure 7b, Well 1, located 1500 m from the shoreline, is reached by salt contamination, which is in agreement with the field observations. The breakthrough curves of salt concentration at the two wells are depicted in Figure 8. In this figure, a small inflection is observed in 2020 when pumping is stopped at Well 1. Then, the concentration continues to increase because of the advancement of the salt front caused by the pumping in Well 2. The final concentration in Well 1 is very high and reaches 30 $g.l^{-1}$. Well 2, located 3000 m from

610 the shoreline, starts to be salinized at around 2060. Then, the concentration continues to
611 increase significantly, with a high rate of salinization, which makes the well unusable in 2070
612 and onward.

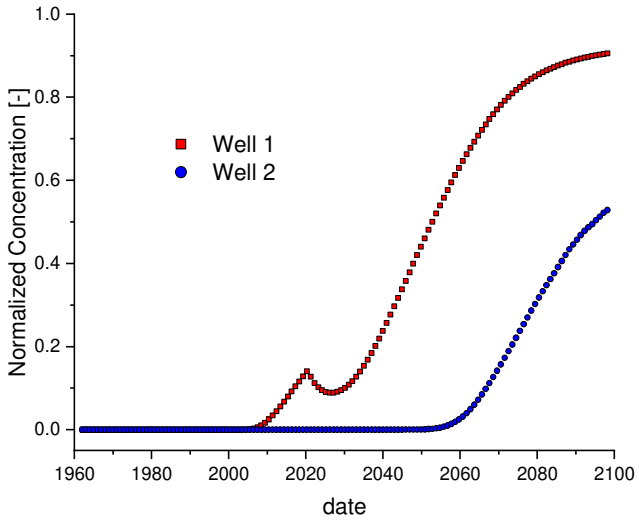

613

614 **Figure 8.** Dimensionless concentration (concentration/seawater concentration) at the two
615 pumping wells.
616
617 Figure 7b shows that the water table slightly falls in 2020 due to pumping. The major part of
618 the aquifer is contaminated by salt in 2100 (Figure 7c) because of (*i*) the reduced recharge
619 caused by climate change and (*ii*) the increase of the pumping rate of Well 2 due to the
620 expected increase of water demand. The progress of saltwater intrusion inside the aquifer is
621 relatively fast, as can be observed in Figure 9, which depicts the evolution of L_{toe} (i.e. the
622 maximum horizontal distance between the shoreline and the 50% salt concentration contour
623 line). The evolution of L_{toe} is almost linear until 2070. The saltwater intrusion is significant
624 and fast. From Figure 9, the salt front invades the domain, with an almost constant velocity of
625 25 $m.y^{-1}$.

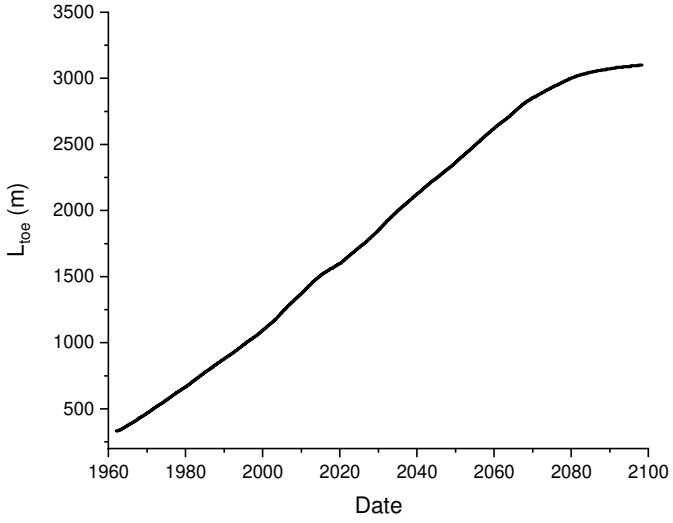

626

627 **Figure 9.** Evolution of L_{toe} (the maximum horizontal distance between the shoreline and the
628 50% salt concentration contour).
629
630 Finally, note that the predicted state in 2100 (Figure 7c) shows that a significant water table
631 falls more than 20 m, which warrants the use of that saturated-unsaturated model to
632 investigate problems of density-driven flow in unconfined coastal aquifers.

633 ## 5. Conclusion

634 Unsaturated–saturated aquifer systems can be subject to pollution by dense contaminants such
635 as SWI in coastal unconfined aquifers. Modeling such problems requires the solution of a
636 highly nonlinear system combining the nonlinear Richards' equation with the advection-
637 dispersion transport equation. The solution of such a nonlinear system can be hampered by
638 convergence issues and excessive computational time, especially for regional-scale problems.
639 A new model has been developed in this work based on advanced spatial discretization
640 methods (lumped MHFE, implicit DG and MPFA methods) and higher-order time integration
641 techniques via the method of lines.

642 The efficiency and accuracy of the new model have been investigated for three test cases. The
643 first test case deals with the infiltration of a contaminant in an unsaturated-saturated

644 rectangular sandbox. This test case served as a benchmark to validate the numerical model.
645 The results of simulations are similar to those obtained with COMSOL. Tracer and dense
646 contaminants yielded similar plumes in the unsaturated zone. However, when the water table
647 is reached, the dense contaminant moves downward, creating a recirculation zone, whereas
648 the tracer moves horizontally along the water table. The test case shows that the new model is
649 highly efficient since it uses large time steps and maintains the same Jacobian for several
650 calculations.

651 The second test case deals with the challenging problem of infiltration into a heterogeneous
652 and initially very dry soil. For this problem, COMSOL failed to reproduce the sharp pressure
653 front and generated strong unphysical oscillations. The new model gives accurate results, and
654 the higher-order integration method is around 7 times more efficient than the classical first-
655 order method.

656 Finally, the developed model has been used to simulate a simplified 2D conceptual model of
657 SWI in the Akkar unconfined aquifer, under climate change and long-term pumping regimes.
658 The purpose of this last test case was to show the applicability of the newly developed model
659 in simulating large-scale regional problems under dynamic conditions. The results show that
660 SWI was moderate in the case of natural equilibrium (in 1962). Then, because of the pumping
661 undergone in the past decades, a significant SWI occurred and salinization reached the
662 pumping well at 1500 m. Simulations until 2100 show that the reduced recharge caused by
663 climate change and the increase in pumping due to the evolution of water demand induce
664 significant salinization of the aquifer, with a salt front advancing inland at an average speed of
665 25 $m.y^{-1}$ and an important water table fall. Note that these preliminary results must be taken
666 with caution since the simulations were performed on a simplified 2D conceptual model
667 without any calibration because of the lack of data.

This study points out that the newly developed numerical model is an interesting tool to assess environmental issues. Efficient and robust numerical models are useful for applications at large scales, involving repetitive simulations, as in model calibration, sensitivity/uncertainty analysis, and scenario-based studies.

Acknowledgments

The authors wish to thank the Investissements d'Avenir and ADEME for supporting this work as part of the GEOTREF research project.

Marwan Fahs would like to acknowledge the support from the National School of Water and Environmental Engineering of Strasbourg through the research project PORO6100.

679 **REFERENCES**

680

681 [1] Diersch, H.J., Kolditz, O., 2002. Variable-density flow and transport in porous media:
682 approaches and challenges. Advances in Water Resources 25, 899-944.
683 [2] Simmons, C.T., 2005. Variable-density groundwater flow: From current challenges to
684 future possibilities. Hydrogeology Journal 13, 116-119.
685 [3] Graf, T., Simmons, C.T., Boufadel, M.C., Neuweiler, I., 2010. Movement of dense
686 plumes in variably saturated porous media: numerical model and results. Proceedings of
687 the XVIII International Conference on Water Resources (CMWR), Barcelona, Spain,
688 June 2010. Abstract 23.
689 [4] Werner, A.D., Bakker, M., Post, V.E.A., Vandenbohede, A., Lu, C., Ataie-Ashtiani, B.,
690 et al., 2013. Seawater intrusion processes, investigation and management: Recent
691 advances and future challenges. Advances in Water Resources, 51, 3–26.
692 [5] Simmons, C.T., Pierini, M.L., Hutson, J.L., 2002. Laboratory investigation of variable
693 density flow and solute transport in unsaturated-saturated porous media. Transport in
694 Porous Media, 47, 215-244.
695 [6] Oostrom, M., Hayworth, J. S., Dane, J. H. and Guven, O., 1992. Behaviour of dense
696 aqueous phase leachate plumes in homogeneous porous media. Water Resources
697 Research 28(8), 2123–2134.
698 [7] Dane, F.H., Guven, O., Oostrom, M., Hayworth, J. S. and Leijnse, A., 1994. Dense
699 aqueous phase contaminant plume behaviour in porous media near the groundwater
700 table. IAHS Publ. 222,333–340.
701 [8] Ouyang, Y., Zheng, C., 1999. Density-driven transport of dissolved chemicals through
702 unsaturated soil, Soil Science 164(6), 376–390.
703 [9] Boufadel, M.C., Suidan, M.T. and Venosa, A.D., 1999. Numerical modeling of water
704 flow below dry salt lakes: effect of capillarity and viscosity. Journal of Hydrology 221,
705 55–74.
706 [10] America, I., Zhang, C., Werner, A. D., & van der Zee Sjoerd E. A. T. M. (2020).
707 Evaporation and salt accumulation effects on riparian freshwater lenses. Water
708 Resources Research, 56, e2019WR026380. https://doi.org/10.1029/2019WR026380
709 [11] Werner, A.D., Lockington, D.A., 2004. The potential for soil salinization above aquifers
710 impacted by seawater intrusion, in Proceedings of 13th International Soil Conservation
711 Organisation Conference: Conserving Soil and Water for Society: Sharing Solutions,
712 edited by S. R. Raine et al., 6 pp., ASSSI/IECA, Brisbane.
713 [12] Werner, A.D., Lockington, D.A., 2006. Tidal impacts on riparian salinities near
714 estuaries. Journal of Hydrology 328, 511–522.
715 [13] Ibrahimi, M.K., Miyazaki, T., Nishimura, T., Imoto, H., 2014. Contribution of shallow
716 groundwater rapid fluctuation to soil salinization under arid and semiarid climate.
717 Arabian Journal of Geosciences 7, 3901–3911.
718 [14] Badaruddin, S., Werner, A.D., Morgan, L.K., 2015. Water table salinization due to
719 seawater intrusion. Water Resources Research 51, 8397–8408.
720 [15] Qu, W., Li, H., Wan, L., Wang, X., Jiang, X., 2014. Numerical simulations of steady-
721 state salinity distribution and submarine groundwater discharges in homogeneous
722 anisotropic coastal aquifers, Advances in Water Resources. 74, 318-328.
723 [16] Zhou, P., Li, G., Lu, Y., Li, M., 2014. Numerical modeling of the effects of beach slope
724 on water-table fluctuation in the unconfined aquifer of Donghai Island, China.
725 Hydrogeology Journal 22, 383–96.
726 [17] Ataie-Ashtiani, B., Volker, R.E., Lockington D.A., 2001. Tidal effects on groundwater
727 dynamics in unconfined aquifers. Hydrological Processes 15, 655–69.

728 [18] Farthing, M.W., Ogden, F.L., 2017. Numerical Solution of Richards' Equation: A
729 Review of Advances and Challenges. Soil Science Society of America Journal 81, 1257.
730 [19] Szymkiewicz, A., 2013. Modelling Water Flow in Unsaturated Porous Media,
731 GeoPlanet: Earth and Planetary Sciences. Springer Berlin Heidelberg, Berlin,
732 Heidelberg.
733 [20] Zha, Y., Yang, J., Yin, L., Zhang, Y., Zeng, W., Shi, L., 2017. A modified Picard
734 iteration scheme for overcoming numerical difficulties of simulating infiltration into dry
735 soil. Journal of Hydrology 551, 56–69.
736 [21] Durlofsky, L., 1994. Accuracy of mixed and control volume finite element
737 approximations to darcy velocity and related quantities. Water Resources Research
738 30(4), 965–974.
739 [22] Schneider, M., Glaser, D., Flemisch, B., Helmig, R., 2018. Comparison of finite-volume
740 schemes for diffusion problems. Oil & Gas Science and Technology - Rev. IFP
741 Energies nouvelles 73, 82.
742 [23] Konz, M., Ackerer, P., Younes, A., Huggenberger, P., Zechner, E., 2009. 2D Stable
743 Layered Laboratory-scale Experiments for Testing Density-coupled Flow Models.
744 Water Resources research 45,W02404.
745 [24] Younes, A., Ackerer, P., 2010. Empirical vs. time stepping with embedded error control
746 for density-driven flow in porous media. Water Resources research 46(8).
747 [25] Chavent, G., Roberts, J.-E., 1991. A unified physical presentation of mixed, mixed-
748 hybrid finite element method and standard finite difference approximations for the
749 determination of velocities in water flow problems. Advances in Water Resources
750 14(6), 329– 348.
751 [26] Younes, A., Ackerer, P., Delay, F., 2010. Mixed finite element for solving 2D diffusion-
752 type equations. Reviews of Geophysics, 48(1).
753 [27] Younes, A., Ackerer, P., Lehmann, F., 2006. A new mass lumping scheme for the
754 mixed hybrid finite element method. International Journal for Numerical Methods in
755 Engineering 67(1), 89-107.
756 [28] Belfort, B., Ramasomanan, F., Younes, A., Lehmann, F., 2009. An efficient Lumped
757 Mixed Hybrid Finite Element Formulation for variably saturated groundwater flow.
758 Vadose Zone Journal. 8, 352-362.
759 [29] Younes, A., Ackerer, P., 2008. Solving the Advection-Dispersion Equation with
760 Discontinuous Galerkin and Multipoint Flux Approximation methods on unstructured
761 meshes. International Journal for Numerical Methods in Fluids 58(6), 687-708.
762 [30] Siegel, P, Mosé, R, Ackerer, P, Jaffré, J., 1997. Solution of the advection-diffusion
763 equation using a combination of discontinuous and mixed finite elements. International
764 Journal for Numerical Methods in Fluids 24, 595-613.
765 [31] Ackerer, P., Younes, A., Mosé, R., 1999. Modelling variable density flow and solute
766 transport in porous medium: 1. Numerical model and verification. Transport in Porous
767 Media 35, 345-373.
768 [32] Hoteit, H., Firoozabadi, A., 2005. Multicomponent fluid flow by discontinuous Galerkin
769 and mixed methods in unfractured and fractured media. Water Resources Research.
770 41(11).
771 [33] Aavatsmark, I., Barkve, T., Bøe, O., & Mannseth, T., 1998. Discretization on
772 unstructured grids for inhomogeneous, anisotropic media. Part I: Derivation of the
773 methods. SIAM Journal on Scientific Computing 19(5), 1700-1716.
774 [34] Younes, A., Fontaine, V., 2008. Hybrid and Multi Point Formulations of the Lowest
775 Order Mixed Methods for Darcy's Flow on Triangles. International Journal for
776 Numerical Methods in Fluids 58(9), 1041-1062.

[35] Ackerer, P., Younes, A., 2008. Efficient approximations for the simulation of density driven flow in porous media. Advances in Water Resources 31(1), 15-27.
[36] Fahs, M., Younes, A., Lehmann, F., 2009. An easy and efficient combination of the Mixed Finite Element Method and the Method of Lines for the resolution of Richards' Equation. Environmental Modelling & Software 24(9), 1122-1126.
[37] Younes, A., Fahs, M., Ahmed, S., 2009. Solving density driven flow problems with efficient spatial discretizations and higher-order time integration methods. Advances in Water Resources 32(3), 340-352.
[38] Van Keken, P.E., Yuen, D.A., Petzold, L.R., 1995. DASPK: A new high order and adaptive time-integration technique with applications to mantle convection with strongly temperature-and pressure-dependent rheology. Geophysical & Astrophysical Fluid Dynamics 80(1-2), 57-74.
[39] van Genuchten, M.Th., 1980. A Closed-form Equation for Predicting the Hydraulic Conductivity of Unsaturated Soils. Soil Science Society of America Journal 44(5), 892-898.
[40] Mualem, Y., 1976. A new model for predicting the hydraulic conductivity of unsaturated porous media. Water Resources Research 12, 513–522.
[41] Raviart, P.A., Thomas, J.M., 1977. A mixed finite element method for second order elliptic problems, in Mathematical Aspects of Finite Element Method. Lecture Notes in Mathematics 606, 292-315.
[42] Younes, A., Ackerer, P., Chavent, G., 2004. From mixed finite elements to finite volumes for elliptic PDE in 2 and 3 dimensions. International Journal for Numerical Methods in Engineering, 59, 365–388.
[43] Moortgat, J., Firoozabadi, A., 2016. Mixed-hybrid and vertex-discontinuous-Galerkin finite element modeling of multiphase compositional flow on 3D unstructured grids. Journal of Computational Physics 315, 476-500.
[44] Vohralík, M., 2006. Equivalence between lowest-order mixed finite element and multi-point finite volume methods on simplicial meshes. Mathematical Modelling and Numerical Analysis 40 (2), 367-391.
[45] Farthing, M.W., Kees, C.E., Miller, C.T., 2002. Mixed finite element methods and higher-order temporal approximations. Advances in Water Resources 25, 85-101.
[46] Tocci, M.D., Kelly, C.T., Miller, C.T., 1997. Accurate and economical solution of the pressure-head form of Richards' equation by the method of lines. Advances in Water Resources 20, 1–14.
[47] Kavetski, D., Binning, P., Sloan, S.W., 2001. Adaptative backward Euler time stepping with truncation error control for numerical modelling of unsaturated fluid flow. International Journal for Numerical Methods in Engineering 53,1301–1322.
[48] Kees, C.E., Miller, C.T., 2002. Higher order time integration methods for two-phase flow. Advances in Water Resources 25(2), 159-177.
[49] Brenan KE, Campbell SL, Petzold LR., 1996. The numerical solution of initial value problems in differential–algebraic equations. Philadelphia, PA: Society for Industrial and Applied Mathematics.
[50] Hindmarsh, A.C., Petzold, L.R., 1995. Algorithms and software for ordinary differential equations and differential-algebraic equations, Part II: Higher-order methods and software packages Computers in Physics 9(2), 148-155.
[51] Curtis, A.R., Powell, M.J.D., Reid, J.K., 1974. On the Estimation of Sparse Jacobian Matrices. Journal of the Institute of Mathematical Applications 13, 117-119.
[52] Hindmarsh, A.C., 1982. Large ordinary differential equation systems and software. IEEE Control System Magazine 2, 24-30.

826 [53] Vauclin, M., Khanji, D., Vachaud, G., 1979. Experimental and numerical study of a
827 transient, two-dimensional unsaturated-saturated water table recharge problem. Water
828 Resources Research 15, 1089–1101.
829 [54] Forsyth, P.A., Kropinski, M.C., 1997. Monotonicity considerations for saturated-
830 unsaturated subsurface flow. SIAM Journal on Scientific Computing 18, 1328-1354.
831 [55] Huang, K., Mohanty, B.P., van Genuchten, M.T., 1996. A new convergence criterion
832 for the modified Picard iteration method to solve the variably saturated flow equation.
833 Journal of Hydrology 178(1-4), 69-91.
834 [56] United Nations Development Program. Assessment of Groundwater Resources of
835 Lebanon. Ministry of Energy and Water, Beirut, Lebanon.2014.
836 [57] Van Vuuren, D., Edmonds, J., Kainuma, M., Riahi, K., Thomson, A., Hibbard, K.,
837 2011. The representative concentration pathways: an overview. Climatic Change 109, 5-
838 31.
839 [58] FAO., 1970. Projet de Développement Hydro-Agricole: Etude Hydrogeologique De La
840 Plaine D'Akkar. République Libanaise, Ministère des Ressources Hydrauliques et
841 Électriques, Beyrouth, Liban.
842
843

844